Exp Fluids (2009) 46:27–41
DOI 10.1007/s00348-008-0534-0

RESEARCH ARTICLE

Temperature response of turbulent premixed flames to inlet velocity oscillations

B. Ayoola · G. Hartung · C. A. Armitage · J. Hult · R. S. Cant · C. F. Kaminski

Received: 13 June 2007 / Revised: 8 June 2008 / Accepted: 10 June 2008 / Published online: 1 July 2008

Abstract Flame–turbulence interactions are at the heart of modern combustion research as they have a major influence on efficiency, stability of operation and pollutant emissions. The problem remains a formidable challenge, and predictive modelling and the implementation of active control measures both rely on further fundamental measurements. Model burners with simple geometry offer an opportunity for the isolation and detailed study of phenomena that take place in real-world combustors, in an environment conducive to the application of advanced laser diagnostic tools. Lean premixed combustion conditions are currently of greatest interest since these are able to provide low NO_x and improved increased fuel economy, which in turn leads to lower CO_2 emissions. This paper presents an experimental investigation of the response of a bluff-body-stabilised flame to periodic inlet fluctuations under lean premixed turbulent conditions. Inlet velocity fluctuations were imposed acoustically using loudspeakers. Spatially resolved heat release rate imaging measurements, using simultaneous planar laser-induced fluorescence (PLIF) of OH and CH_2O, have been performed to explore the periodic heat release rate response to various acoustic forcing amplitudes and frequencies. For the first time we use this method to evaluate flame transfer functions and we compare these results with chemiluminescence measurements. Qualitative thermometry based on two-line OH PLIF was also used to compare the periodic temperature distribution around the flame with the periodic fluctuation of local heat release rate during acoustic forcing cycles.

B. Ayoola · G. Hartung · J. Hult · C. F. Kaminski (✉)
Department of Chemical Engineering, University of Cambridge, Pembroke Street, Cambridge CB2 3RA, UK
e-mail: cfk23@cam.ac.uk

G. Hartung
e-mail: georg.hartung@osram-os.com

C. F. Kaminski
SAOT School of Advanced Optical Technologies, Max Planck Research Group Division III, University Erlangen-Nuremberg, Nuremberg, Germany

C. A. Armitage · R. S. Cant
Department of Engineering, University of Cambridge, Trumpington Road, Cambridge CB2 1PZ, UK

1 Introduction

Many experimental and theoretical studies are currently being undertaken in an effort to gain a better understanding of unsteady flame behaviour in lean premixed combustion. Quantities of major interest include the rate of heat release and temperature. Chemiluminescence is widely applied as a marker of global heat release. It is radiation emitted from electronically excited molecules when these return to a lower energy state. For example, OH* chemiluminescence – peaking near 308 nm – is widely applied in this respect and has been found to serve as a good indicator for global heat release rate in premixed hydrocarbon flames. However, chemiluminescence cannot capture fine scale structure of flames, since the signal is integrated over the whole line-of-sight. Planar laser induced fluorescence (PLIF) does not suffer this disadvantage and offers greatly superior spatial resolution, as measurement data is only obtained from the cross-section of the flame illuminated by the laser sheet. In addition, the signal photon flux in PLIF measurements is much larger than for chemiluminescence and data can therefore be obtained over much shorter integration times, without risk of temporal averaging.

Experimental and theoretical investigations suggest that the formyl radical (HCO) is an excellent indicator of heat release rate in both steady and unsteady lean premixed hydrocarbon flames (Najm et al. 1998; Fayouxa et al. 2005). HCO is one of the final reaction intermediates through which the chemistry proceeds to the production of CO and it thus accounts for a large fraction of the heat-releasing chemical interactions. In principle, HCO can be measured using PLIF, although signal strengths are far too weak to permit single shot measurements to be performed in practical applications. An alternative approach to HCO imaging is to simultaneously record images of formaldehyde (CH_2O) and OH concentrations, both of which are readily obtained by PLIF with good signal-to-noise ratios. The pixel-by-pixel product of OH and CH_2O images correlates well with HCO concentration and thus with heat release rate. The technique, subsequently denoted as heat release rate (HRR)-imaging, has been thoroughly validated in laminar and turbulent flames and has been used to examine flame–vortex interactions in laminar unsteady and turbulent flames (Paul and Najm 1998; Balachandran et al. 2005; Ayoola et al. 2006). These studies suggest that the HRR technique is more reliable than chemiluminescence in measuring heat release rate in flames where strong vortices are present (Ayoola et al. 2006), e.g. in flames were strong thermoacoustic interactions are taking place. In addition, the superior spatial resolution of HRR imaging permits the investigation of localised flame phenomena (e.g. local stretch and curvature) and their effect on the heat release rate.

Another quantity of fundamental importance is local flame temperature which can be determined by a variety of techniques. For example, one can seed the flow with temperature-sensitive tracer molecules such as NO, and perform PLIF on the tracer gas (Lee et al. 1993; Tsujishita et al. 1999). However, such methods may influence flame chemistry. Using natively produced OH radicals circumvents this problem although OH concentrations sufficiently high for PLIF are only present at high temperature (>1,000 K for lean premixed HC flames) (Giezendanner-Thoben et al. 2005a, b). Temperatures are obtained from a ratiometric measurement of the fluorescence signals resulting from involving the sequential excitation from two different energy levels. The ratio of the resulting fluorescence signals can be related to the ratio of the initial-state populations, which in turn can be related to temperature if local thermodynamic equilibrium prevails.

In this paper, we present the application of spatially resolved heat release rate imaging, through the simultaneous application of CH_2O- and OH-PLIF, the measurement of temperature employing OH 2-line thermometry, and finally OH* chemiluminescence monitoring in turbulent lean premixed flames. Experiments were performed in an acoustically forced bluff-body-stabilised burner, which could be operated with or without acoustic forcing. Both the acoustic forcing frequency and the forcing amplitude were varied. A computational study was also carried out using a well-established unsteady Reynolds–Averaged Navier–Stokes (uRANS) approach (Armitage et al. 2006). Previous uRANS results for heat release have been complemented by validation of the computed temperature field against the newly obtained experimental data. Although the computational data set is preliminary and are not the main emphasis of the paper, the results provide an illustration of the more general usefulness of the experimental data-set for the validation of combustion CFD.

The combined heat release rate and temperature data could also be used to evaluate flame transfer functions, which are commonly used in the study of combustion instabilities (Lee and Santavicca 2003; Balachandran et al. 2005; Lawn et al. 2004; Lawn and PoLIFke 2004; Dowling and Stow 2003; Pun et al. 2003). For fully premixed fuel/air mixtures the flame transfer function is defined as

$$T_f(f,A) = \frac{q'/\overline{q}}{u'/\overline{U}} \tag{1}$$

where $q(t) = \overline{q} + q'(t)$ and $U(t) = \overline{U} + u'(t)$; bars denote averages and primes denote fluctuations, q is the heat release rate, U is the bulk gas velocity, f is the frequency and A the amplitude of the inlet velocity fluctuations. The latter is represented as $u'(f)/\overline{U}$. Until now, almost every study on flame transfer functions has been based on chemiluminescence measurements for heat release rate. These include narrow-band OH*, CH* and C_2*, and broadband C_2* chemiluminescence measurements. One aim of the present work is to compare the relative performance of the chemiluminescence and HRR imaging techniques for the calculation of flame transfer functions. To our knowledge this is the first time that data obtained using the HRR technique have been used directly in the calculation of flame transfer functions.

The model burner used was developed to mimic the physics of an instability cycle occurring in a real gas turbine combustor operated under lean premixed conditions. Instabilities are triggered by small variations in equivalence ratio or inlet velocity which in turn act to change the heat release rate q'. This then leads to the production of acoustic waves which can couple to a resonant eigenmode of the combustor geometry. The present work can be seen as part of a wider effort to shed light on the mechanisms of thermoacoustic instability with a view to improving predictive capabilities and the development of active control strategies (Dowling and Morgans 2005). The same burner has been the subject of several related studies. Balachandran et al. (2005) investigated the nonlinear response of the flame by performing integrated heat release rate

measurements by means of OH* and CH* chemiluminescence. In addition, PLIF of OH was carried out from which the phase resolved flame surface density was computed. Hartung et al. (2008) and Hartung (2008) carried out simultaneous stereoscopic particle imaging velocimetry and time-sequenced OH-PLIF in this burner in order to measure local flame displacement speeds and alignment statistics of principal strains.

The outline of the paper is as follows. First, the implementation of the relevant imaging and image processing techniques are discussed. Second, results from the bluff-body-stabilised flame are presented and the heat release response to a varying amplitude of forcing is shown. Correlations are presented between heat release fluctuations and temperature. A comparison with results from the uRANS calculations is then presented. Finally, flame transfer functions obtained from heat release rate measurements are compared to those obtained from OH* chemiluminescence measurements.

2 Experimental methods

2.1 Heat release rate imaging

In recent studies the production rate of the formyl radical (HCO) has been found to be a good measure of heat release rate because HCO lies on the major pathways for the production of CO from hydrocarbons. However, HCO is difficult to image with LIF because its accessible electronic transitions are predissociative (Eckbreth 1996). The fluorescence signals are also strongly quenched, all resulting in very short excited state lifetimes. Since HCO is formed according to Eq. (2) an alternative approach uses the product of simultaneous OH and CH_2O PLIF measurements to obtain a signal that correlates with HCO production rate.

$$CH_2O + OH \rightarrow HCO + H_2O \tag{2}$$

This is possible because the removal rate of the highly reactive formyl radical is significantly faster than its production rate, and hence the HCO concentration is directly proportional to its production rate. The spectroscopic methodology of this imaging technique has been described and demonstrated by Paul and Najm (1998), Vagelopoulos and Frank (2005) and Ayoola et al. (2006). The forward rate of this reaction is $k(T)[CH_2O][OH]$, where k is the rate constant, T is temperature, and the square brackets denote number densities. The LIF signals are related to species densities with a dependence on the local composition and temperature T that results from variations in the collisional quenching rates and Boltzmann population fraction. The product of simultaneously recorded LIF signals of CH_2O and OH can therefore be expressed as

$$\mathrm{LIF}(CH_2O) \times \mathrm{LIF}(OH) = f(T)[CH_2O][OH] \tag{3}$$

where $f(T)$ represents the combined temperature dependence of the CH_2O and OH LIF signals. At a constant equivalence ratio Φ, and over a limited range of temperature T, it is possible to select transition lines such that $f(T)$ is proportional to the forward rate constant $k(T)$ of the reaction in Eq. (2). As a result, the product of the LIF signals is proportional to the reaction rate. Overlapping transitions were selected near the bandhead of the $\tilde{A}^1A_2 - \tilde{X}^1A_14_0^1$ system near 353 nm for CH_2O and the $Q_1(6)$ transition in the $A^2\,\Sigma^+ - X^2\,\Pi(1,0)$ band near 283 nm for OH. Numerical simulations providing evidence for the validity of the reaction rate imaging scheme for these transitions can be found elsewhere (Ayoola et al. 2006).

2.2 OH two-line thermometry

The principle of OH two-line thermometry is to measure the relative populations of two states using linear excitation to an identical upper state (Palmer and Hanson 1996) and to calculate the temperature via a Boltzmann expression as given below,

$$R = C\left(\frac{V_{c1}}{V_{c2}}\frac{B_1}{B_2}\frac{I_{v1}}{I_{v2}}\frac{\phi_{fe1}}{\phi_{fe2}}\right)\frac{(2J_1+1)}{(2J_2+1)}e^{-\frac{E_1-E_2}{k_BT}} \tag{4}$$

where R is the ratio of the two fluorescence signals, C a calibration constant, V_{ci} the fluorescence collection volume, B_i the Einstein coefficient for absorption, ϕ_{fe} the fluorescence quantum yield, I_{vi} the laser spectral irradiance, J_i the rotational angular momentum quantum number, E_i is the energy state of i, k_B is Boltzmann's constant and T is the temperature.

Since the combustion of a lean ethylene–air mixture, which was used for the experiments described in this paper, produces temperatures between ambient and 1,600 K, the transition lines employed in this technique were chosen to be highly temperature sensitive in this temperature range. In order to identify these lines, a simulation of the LIF signals for a selection of transition lines between various energy levels in the OH radical was performed using the rotational level dependence of the collisional quenching rates obtained from Crosley (1981). From Eq. (4), it can be seen that a large energy difference increases the exponential term, thereby increasing the signal ratio R. Consequently, Cattolica and Stephenson (1986) excited OH transitions from different vibrational energy levels; the $Q_1(5.5)$ line in the (1,0) and (1,1) vibrational bands within the $A^2\,\Sigma^+ - X^2\,\Pi$ electronic transitions allowing temperatures up to 5,000 K to be measured. The two lines that were

used in this work, however, were from the same vibrational band, since sensitivity was desired between 700 and 2,000 K. If the transition lines probed are within the same vibrational band and only differ in rotational quantum number, the temperature measurements will yield a rotational temperature. In atmospheric pressure flames, this is an advantage, as equilibrium is rapidly achieved with the thermodynamic translational temperature of the gas via molecular collisions and rotational re-distributions. An optimal pair from the (1,0) vibrational band was selected by ensuring that the transition lines differ only in rotational quantum number, give good signal strengths, are isolated from other transitions, and are highly sensitive from 700 to 2,000 K. The chosen pair are the $P_1(1.5)$ and $Q_1(5.5)$ (Palmer and Hanson 1996) lines within the $A^2\ \Sigma^+ - X^2\ \Pi$ electronic transition of OH. Figure 1 shows the simulated profile of the fluorescence ratio R, as a function of temperature for this transition pair along with other pairs considered.

The $R_1(12.5)$:$P_1(7.5)$ line pair also features good temperature sensitivity within the stated temperature range, however, the populations in these rotational levels are low compared with the $Q_1(5.5)$:$P_1(1.5)$ line pair for temperatures from 800 to 1,600 K. This is a disadvantage in atmospheric pressure flames where high fluorescence signals are desired for quantitative measurements. Similar transitions were employed by Palmer and Hanson (1996) to perform temperature measurements in a supersonic jet flame of hydrogen and oxygen diluted with argon.

In order to determine the calibration constant C, temperature measurements were performed in a laminar premixed Bunsen C_2H_4/air flame at $\Phi = 1.4$, and were compared to one-dimensional flame simulations calculated using the PREMIX code for the same flow conditions (Kee et al. 1993). The calibration was performed at this equivalence ratio because premixed C_2H_4 flames at equivalence ratios lower than 1.4 could not be stabilised on our laminar Bunsen burner. A value of $C = 1.10 \pm 0.2$ was obtained and applied in Eq. 4. For the purpose of the current work temperature data was used to compare the structural dynamics of the flame as observed with the different techniques employed, e.g. heat release rate imaging and the URANS model results presented later on. As such the emphasis was less on a full quantification of the temperature fields than on a capture of global trends. Over the regions imaged OH concentrations could vary by orders of magnitude within images because (a) the OH production rates are dependent on temperature in a highly non-linear fashion, and (b) because OH concentrations are dramatically diminished by mixing with reactant and product gases, etc. In what follows we quote precision as that relating to regions in images were signal to noise ratios are lowest. Overall error estimates are thus conservative: near the flame front, where OH concentrations are much higher, temperatures are significantly more precise than what is quoted as an error throughout the paper. It is, however, again worth to emphasize that the thermometry data is used in a qualitative fashion to obtain phenomenological insight.

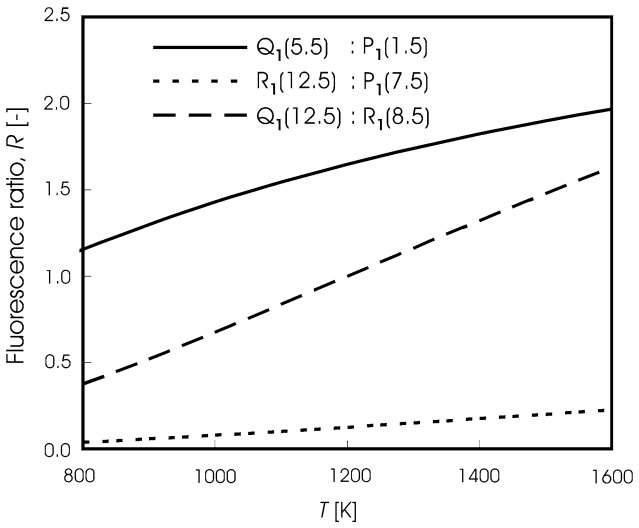

Fig. 1 Fluorescence signal ratio R with increasing temperatures for three pairs of transition lines in the (1,0) vibrational band of the $A^2\ \Sigma^+ - X^2\ \Pi(1,0)$ electronic transition in OH

2.3 OH* chemiluminescence

Chemiluminescence is the radiative emission given off by electronically excited reactive species and is extensively used as an indicator of global heat release rate in premixed hydrocarbon flames. The strongest chemiluminescence emitters in lean hydrocarbon combustion are OH*, CH*, and CO^*_2, and all have been used as indicators of global heat release rate and their relative merits and drawbacks discussed (Lee and Santavicca 2003; Samaniego et al. 1995). For OH*, which was used in the present study, the peak of the $A^2\ \Sigma$ emission occurs at 310 ± 10 nm; hence, OH* can be collected using UV-sensitive CCD cameras. Our measurements of OH* include a small contribution from CO^*_2 (~10%) because CO^*_2 has a broadband emission spectrum extending from 350 to 600 nm; however, the effect of this on OH* signals is significantly reduced by the narrow-band collection of the OH* chemiluminescence signals (usage of same filter set-up as for OH-PLIF). The ICCD-camera was gated for 50 μs and 75 images were averaged before calculating the Abel-transformed OH*-image.

2.4 Burner

For this investigation, a 10-kW laboratory scale bluff-body-stabilised burner was designed. It was made up of a

circular duct 300 mm long with an inner diameter of 35 mm. The conical bluff-body anchoring the flame was 25 mm in diameter, giving a blockage ratio of 50%. In order to mimic combustion instabilities on a simple, well-controlled system, inlet velocity fluctuations were imposed on the bluff-body flame using two acoustic drivers (loudspeakers) mounted diametrically opposite each other on the circumference of the burner plenum. The loudspeakers were excited with sinusoidal signals from a waveform generator (TGA 1242, TTi, UK). The flame was acoustically forced at an eigenmode of the plenum chamber which was 160 Hz. At this forcing frequency, a fluctuation amplitude of 65% of the mean inlet velocity was achieved. Experiments were carried out with the combustor operating on premixed C_2H_4 and air at an equivalence ratio of 0.55 (Le $>$ 1). The flame was enclosed in a fused silica quartz cylinder to ensure that there was no entrainment of atmospheric air, which would cause local variations in equivalence ratio. A schematic representation of the combustor and an image of the quartz enclosure and the bluff-body are shown in Fig. 2. Full details and a characterisation of the burner can be found in Balachandran et al. (2005).

In this paper, measurements were made for seven different bluff-body-stabilised flame configurations as described in Table 1. In this table, flames 1 to 5 were acoustically forced flame at a frequency f at 160 Hz. Flames 6 and 7 were forced at other eigenmodes of the combustion chamber (40 and 310 Hz). The forcing amplitude was varied over 4 different magnitudes over the mean inlet velocity, which were $\Delta u/\bar{u} = 0.12, 0.32, 0.55$ and 0.65. Flames 2 to 5 allow the amplitude response of the acoustically forced flame to be investigated; a comparison of flames 6, 5 and 7 provides insight into the frequency response of the flame. The bulk velocity for flame 1 is 13.0 m/s, which results in conditions very close to global extinction. Flames 2 to 7 employ a bulk velocity of 9.9 m/s, which corresponds to a lower global strain rate than flame 1. All flames investigated were operated at an equivalence ratio of 0.55.

An illustration of the velocity contours at the burner exit superimposed on a planar image of OH fluorescence is shown in Fig. 3. The flame conditions were $\Phi = 0.55$, bulk velocity = 9.9 m/s and Re = 19,000. The velocity contours illustrated here were obtained from laser Doppler velocimetry measurements (Ayoola 2006). The velocity contours show both an inner recirculation zone and an outer recirculation zone in the wake region behind the bluff-body and the flames are stabilised at the shear layer by the recirculation of hot products.

At higher equivalence ratios, the single flame front stabilised by the inner shear layer is unable to consume all the premixed reactants. Thus, a second flame front is stabilised by the outer recirculation zone at the outer shear layer, as indicated in 3.

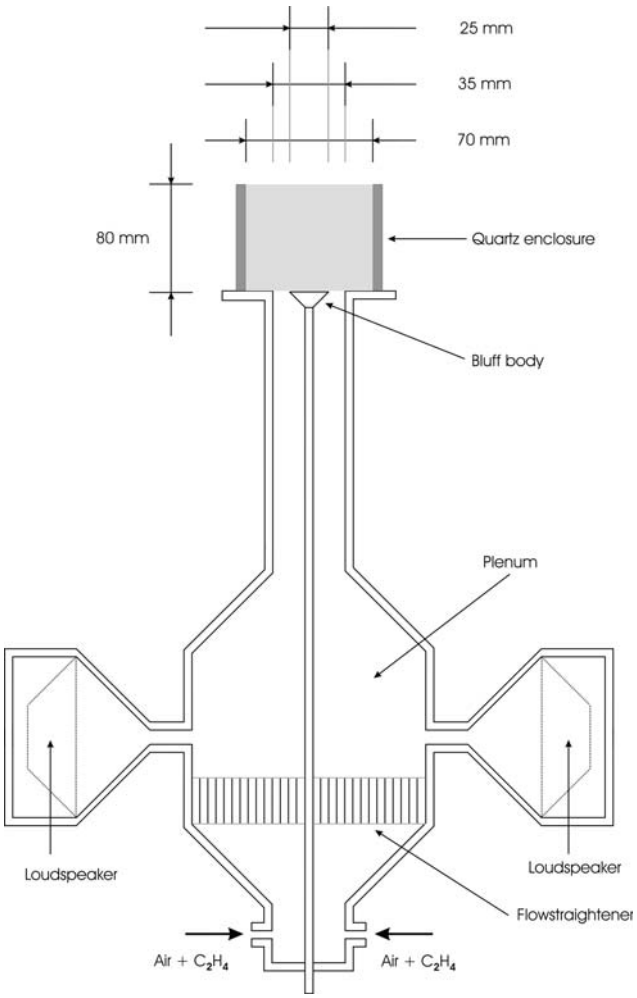

Fig. 2 Schematic of the acoustically forced bluff-body burner (Balachandran et al. 2005)

Table 1 Summary of the operating conditions for the lean ethylene-air flames investigated in the bluff-body-stabilised burner

Flames no.	Forcing freq. f (Hz)	forcing amplitude $\Delta u/\bar{u}$ (–)	Φ	Axial vel. v_y (m/s)	Reynolds no. Re (–)
Flame 1	160	0.65	0.55	13.0	25,000
Flame 2	160	0.12	0.55	9.9	19,000
Flame 3	160	0.32	0.55	9.9	19,000
Flame 4	160	0.55	0.55	9.9	19,000
Flame 5	160	0.65	0.55	9.9	19,000
Flame 6	40	0.65	0.55	9.9	19,000
Flame 7	310	0.65	0.55	9.9	19,000

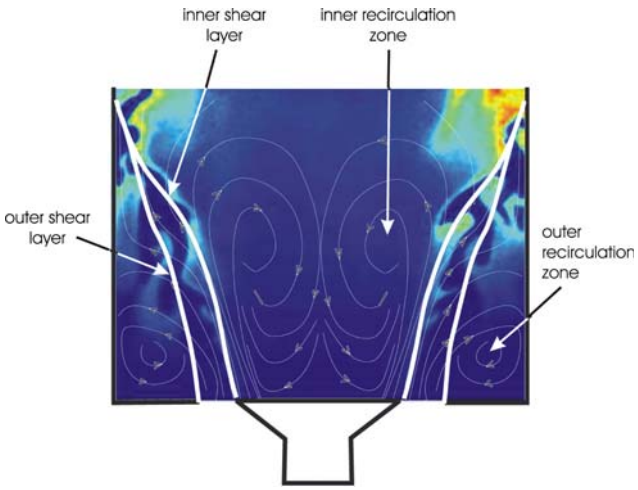

Fig. 3 Illustration of the velocities at the burner exit superimposed on a single shot OH-PLIF image (flame conditions: $\Phi = 0.55$, bulk velocity = 9.9 m/s, *Re* = 19,000) (Ayoola 2006)

2.5 Diagnostic apparatus

The diagnostic system consisted of two Nd:YAG lasers (Continuum Surelite) used as pump sources for two tunable dye lasers [Sirah Cobra–Stretch, (linewidth 0.0027 nm)]. Two high-resolution double-exposure ICCD cameras (La-vision Nanostar) were used for the digital collection of the fluorescence signals.

2.5.1 *Heat release rate imaging, OH-two-line thermometry and OH* chemiluminescence*

Figure 4a shows a schematic of the diagnostic set-up for heat release rate imaging. The diagnostic set-up has been described in detail elsewhere (Ayoola et al. 2006).

2.5.2 *OH two-line thermometry*

The cameras for imaging both OH PLIF laser sheets were fitted with UV f/4.5 camera lenses (Nikkor) equipped with UG 11 and WG 305 filters (Comar). For spectral identification of the OH transitions, LIF excitation scans were performed for each dye laser prior to the PLIF measurements. For OH LIF, the frequency-doubled output from one dye laser was tuned near 282.2 nm to excite the $P_1(1.5)$ line in the $A^2\ \Sigma^+ - X^2\Pi(1,0)$ band. The frequency-doubled output from the second dye laser was tuned to 282.7 nm to excite the $Q_1(5.5)$ line in the same band. The laser beams were expanded into sheets 50 mm high and 100 μm thick, using negative cylindrical planoconvex lenses with focal lengths of −25 mm and spherical positive lenses with focal lengths of 500 mm. The beams from the dye lasers were spatially filtered, which reduced the pulse energies to less than 2 mJ per pulse in the interaction regions for both OH lines. Linearity checks of the fluorescence signals with laser intensity were performed. A schematic representation of the setup is shown in Fig. 4b. Both ICCD-cameras were capable of acquiring two images in rapid succession. This allowed the measurement of an OH PLIF image (intensifier gated to open for 350 ns) shortly followed by an OH*-emission measurement (gated to open for 50 μs) on the same camera. A delay of 500 ns was chosen between the OH laser pulses to prevent possible interference between the laser pulses and the cameras. The selected delay of 500 ns rendered the PLIF measurements virtually instantaneous on flow timescales at the given bulk velocities and with the spatial resolution of the optical setup.

2.6 Image processing

Raw PLIF images were corrected for background and laser inhomogeneities before the pixel-by-pixel product (heat

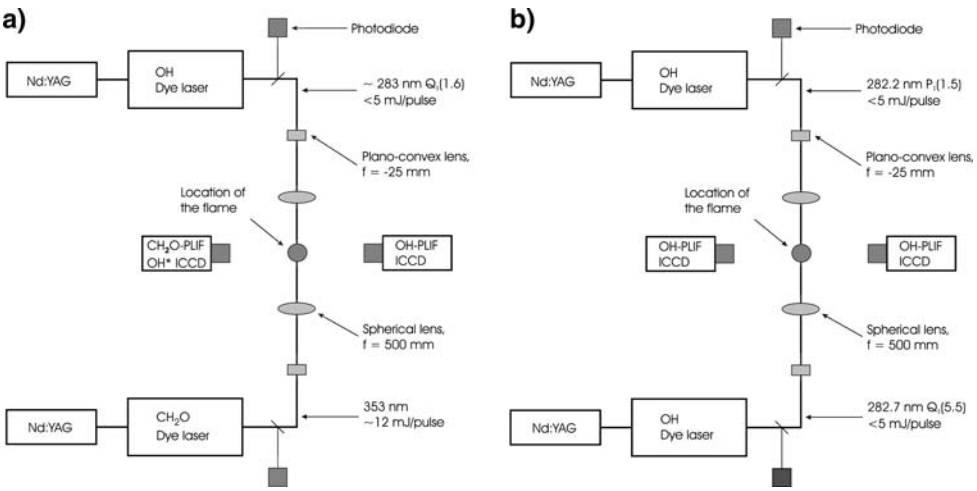

Fig. 4 Schematic of the laser set-up for PLIF measurements: **a** Heat release rate and OH*-chemiluminescence, **b** OH two-line thermometry

release rate imaging) or pixel-by-pixel ratio (two-line thermometry) was calculated to obtain either the heat release rate or the temperature distribution. First, all images were resized to 50% of their original size yielding a signal-to-noise ratio gain of 2. Second, a background image, measured in the absence of the flame, was subtracted from the fluorescence images. Third, the images were corrected for laser-sheet beam profile. This was done by dividing the instantaneous PLIF images by the average beam profiles of the exciting lasers. Before and after each flame measurement the beam profiles for each dye laser were measured in a homogeneous vapor of air-diluted biacetyl (for CH_2O) and acetone (for OH). Finally, both PLIF images were warped onto each other on a pixel-by-pixel basis. This alignment is essential to the success of these imaging techniques because of the small spatial scales of the reacting layers in the flame. This warping procedure was performed in several stages. First, both laser sheets were aligned to pass exactly the same measurement plane. Second, a target image (cross pattern) was aligned in the measurement plane, defined by the laser sheets and in the view of both cameras. Third, the coordinates of several reference points on the target image, captured by the camera 1, were recorded as anchor points. The target was then imaged with the camera 2. For heat release rate imaging camera 1 recorded CH_2O and camera 2 recorded OH [$Q_1(6)$]; for OH two-line thermometry camera 1 recorded OH [$Q_1(5.5)$] and camera 2 recorded OH [$P_1(1.5)$]. The image from camera 2 was mirrored and the corresponding coordinates of the same reference points were identified. Third, a transformation matrix relating the two sets of coordinates was calculated and used to map the images of camera 2 onto the coordinate system of the image 1. This image processing technique is similar to that employed in particle image velocimetry and its precision is in the subpixel range (Jambunathan et al. 1995).

In the case of heat release rate imaging the corrected images were then multiplied on a pixel-by-pixel basis to obtain the heat release rate images; in the case of OH two-line thermometry the corrected images were then divided on a pixel-by-pixel basis and the temperature field was obtained using Eq. (4) to obtain the temperature images. Both cameras had an ICCD chip size of 1,280 × 1,024 pixels and were positioned to give a spatial resolution of 0.07 mm/pixel (after resizing) at the measurement plane. At this high resolution, the spatial distribution of the species being probed is clearly resolved.

2.7 Uncertainty estimate

The major contributors to uncertainty in the measurement of heat release rate with the PLIF technique, and temperature using the two-line method with OH PLIF, is the shot to shot variation of the laser energy and the subtle changes that occur in the laser beam profiles. The fluctuation of laser energy during the period of taking PLIF measurements resulted in a standard deviation of 15% in the spatially integrated OH and CH_2O PLIF images. With this deviation, the uncertainty in the heat release rates and temperatures measured using the PLIF techniques can be estimated by calculating the propagation of errors.

2.7.1 Heat release rate imaging

The measurement of heat release rates is based on the pixel-by-pixel product of simultaneous PLIF images of OH and CH_2O. The uncertainty in the resulting heat release rates can be estimated by combining the errors in the respective PLIF images. The resulting relative uncertainty in the heat release rate images was 20%. Additional systematic uncertainties may be introduced by variations in the local fluorescence quenching environment, and also by beam steering through the turbulent flame which can affect the precision of the pixel-by-pixel mapping. The latter has only a minor effect on the uncertainty as steering is low in the very lean and relatively cool flame. Also steering is very similar for both laser sheets as they pass through identical regions of the flame at almost the same time instance. The evaluation of the first type of error requires temperature and species dependent quenching cross-sections, which are available for OH but are quite limited for CH_2O. However, this error is expected to be relatively modest based on the simulations discussed elsewhere (Ayoola 2006).

2.7.2 OH two-line thermometry

We quote overall uncertainties in the measured flame temperature to be in the order of 20%. This estimate arises from several sources. There are errors in the calibration constant, C, variations in laser energy and beam profile fluctuations (which could not be corrected for on a shot by shot basis in our set-up). The major source of errors comes from the fact that we image over very large fields of view where OH concentrations change by orders of magnitude. Whilst temperatures near the flame fronts are much more precise (owing to the high OH levels and corresponding strong signals) the temperature closer to the bluff body and other low OH level containing regions are severely affected by low signal to noise ratios. Uncertainties were estimated by propagating the errors with the variance s of the two simultaneous OH PLIF signals, and including a variation in C as a result of a proportionate variation in OH quenching rates, estimated from Garland and Crosley (1986). This corresponds to approximate uncertainties of up to ±280 K. These uncertainties are quite large compared with other

thermometry techniques. With such high uncertainties, only qualitative temperatures can be reported. In this work, we study the transport of hot products in the recirculation zone of the bluff-body flame, where it is more important to distinguish between regions of high and low temperatures and to correlate such information with heat release rates in different turbulent flow fields. The optimal measurement of temperature would involve calibrating the two-line method against another measurement technique, but this was not necessary for the qualitative comparisons reported here. It should be noted, however, that we use temperature profiles not for quantitative purposes, but for comparisons of flame structural features with the HRR and URANS data.

2.8 Computational framework

The computational work was carried out using the approach described by Armitage et al. (2006). The governing equations are the compressible Navier Stokes equations together with a transport equation for a reaction progress variable c defined in terms of the fuel mass fraction Y_F:

$$c = \frac{Y_{Fu} - Y_F}{Y_{Fu} - Y_{Fb}}. \tag{5}$$

normalised by the limiting values in the unburnt (u) and burnt (b) states.

The equations are Favre-averaged, assuming implicitly that the time-scale of the turbulence is much smaller than that of the unsteady mean flow field. Closure of the resulting uRANS equations is achieved using a linear Reynolds stress model (Launder et al. 1975) together with a gradient-transport approximation (Daly and Harlow 1970) for the Reynolds fluxes. The mean turbulent reaction rate $\overline{\omega}$ is modelled using the Bray–Moss–Libby laminar flamelet formulation (Bray et al. 1985):

$$\overline{\omega} = \rho_u S_L I_0 \Sigma \tag{6}$$

in which ρ_u is the unburned density, S_L is the unstrained laminar burning velocity, I_0 accounts for the effects of strain and curvature and Σ is the flame surface density. An empirical correlation (Abu-Orf 1996) is used to obtain S_L as a function of equivalence ratio, pressure and unburned temperature while algebraic models (Brookes et al. 1999, 2000) are provided for both I_0 and Σ. Full details are given by Armitage et al. (2006)

For the present axisymmetric problem the closed uRANS equations are formulated in cylindrical co-ordinates and are discretised in space using the bounded second-order CCCT scheme (Gaskell and Lau 1988). First-order Euler implicit time differencing is employed within a modified PISO pressure-correction algorithm (Issa 1986; Watkins et al. 1996). The implementation in the combustion CFD code TARTAN (Li and Cant 1994) has been extensively validated in previous related work (Brookes et al. 1999, 2000; Armitage et al. 2004).

The flame zone above the bluff-body burner was represented using a computational mesh consisting of 70 cells radially by 160 cells axially, giving a 0.5 mm grid resolution over the whole domain. Mesh independence was tested by halving the resolution without significant changes to the solution.

Having first obtained a steady solution, sinusoidal velocity fluctuations were superimposed on the mean inlet velocity while keeping the inlet flow angle constant. The simulation was run until a stable limit cycle was well established, and all results were taken over a minimum of six complete cycles.

3 Results and discussion

The techniques presented in the previous section were used to measure the heat release rate as well as temperature distributions in the forced flames. A presentation of the amplitude and frequency response of the heat release rate to acoustic flame forcing and temparature measurements are given, followed by a comparison of flame transfer functions based on the HRR- and OH* imaging techniques.

3.1 Periodic flame response

3.1.1 HRR and temperature map

Figure 5 shows a sequence of phase-averaged heat release rate and temperature distributions, measured in the bluff-body-stabilised flame forced at 160 Hz with an amplitude fluctuation of 65% over a mean inlet velocity of 13 m/s (flame 1).

The images shown in Fig. 5 (1st row) cover 12 steps through a full acoustic cycle covering phase angles from 0° to 330° in increments of 30°. From top to bottom the two rows in the sequence denote the heat release (HRR) and the measured temperature field (T_{exp}).

From the images it is clear how the inner shear layer wraps around the inner vortex as it convects away from the bluff-body (compare also with Fig. 3). From the temperature images obtained at the corresponding phase angles (2nd and 4th rows) it may be seen that in regions of high curvature, i.e. where the vortex strongly wrinkles the flame front, high temperatures are observed around the vortex, compared to the lower temperatures found within the inner recirculation zone. With the development of the vortex at a phase angle of 60°, the heat release rate reaches a peak as shown in the spatially integrated heat release rate profile in Fig. 6.

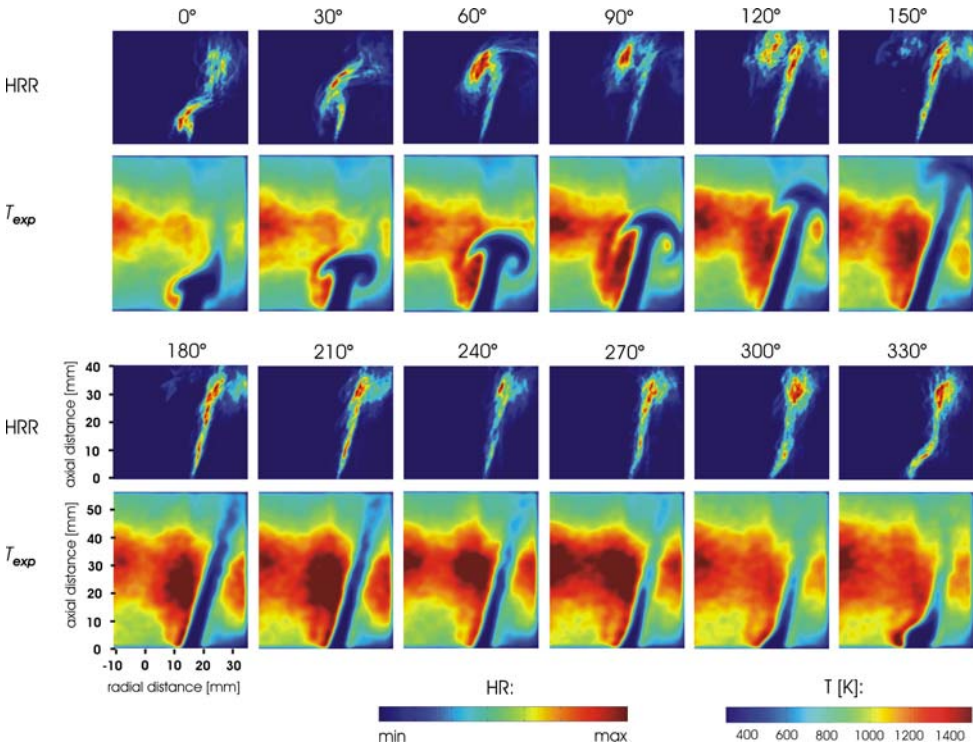

Fig. 5 A sequence of phase-averaged heat release rate (HRR) and temperature images (T_{exp}) measured in the acoustically forced bluff-body-stabilised flame (flame 1, A = 0.65)

However, the maximum extent of the high temperature region does not occur at this phase angle, but later at phase angles 210°–270° (Fig. 5; 4th row), when the flame front and shear layer are no longer wrinkled and the vortex has travelled through the region of interest. This suggests that the intense wrinkling of the flame front by the inner vortex imposes high negative curvatures on the flame and makes a large contribution to the local heat release rate. From the periodic temperature distribution in Fig. 5 (2nd and 4th row), it can be seen that a uniform distribution of high temperatures around the flame front and inner recirculation zone occurs when the flame surface area is at a minimum, at phase angles 210°–270°; conversely, a smaller region of high temperatures was observed when the flame surface area is at a maximum.

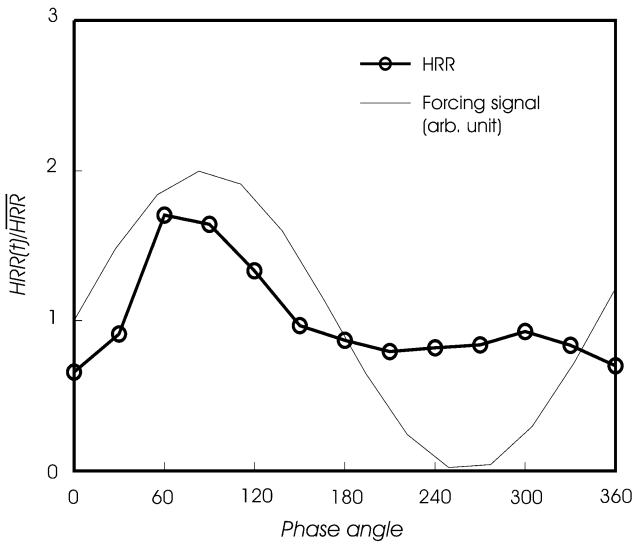

Fig. 6 Cyclic variation of heat release rate in the bluff-body-stabilised flame normalized by the mean ($\overline{HRR}$) : flame 1; A = 0.65

3.1.2 *HRR response for varying forcing frequency*

The flame response as a function of forcing frequency was investigated. Results are presented here for forcing frequencies of 40, 160 and 310 Hz. Measurements were performed at these frequencies because of the high amplitude inlet velocity fluctuations A, possible to be achieved. Each forcing cycle was divided into 12 phases to ensure that the periodic response of the flame through the cycle was resolved.

Figure 7 shows three sequences of phase averaged HRR images measured in the bluff-body stabilized flame, forced at frequencies of 40, 160 and 310 Hz, respectively, with A = 0.65.

The 40-Hz images (1st and 4th row of Fig. 7) reveal that the structure of the flame front is undisturbed by the inlet velocity fluctuations. This implies that the counter-rotating vortex pair, formed at the bluff-body at this forcing frequency, was not strong enough to distort the inner shear layer on which the flame front is stabilized. However, from the sequence of images, we observe that although the propagating vortices do not distort the flame front, the

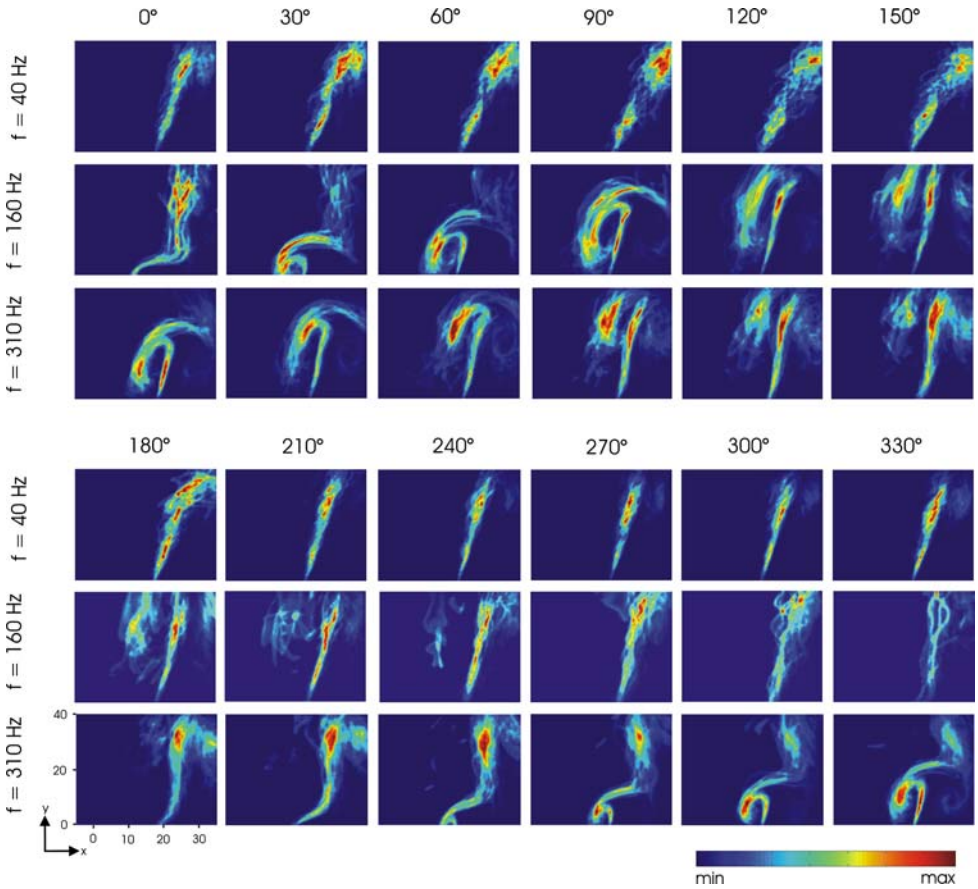

Fig. 7 Three sequences (0° to 330°) of phase averaged heat release rate images for three different forcing frequencies (flame 6: $f = 40$ Hz; flame 5: $f = 160$ Hz, flame 7: $f = 310$ Hz;) measured using the heat release technique in the acoustically forced bluff-body stabilized flame ($A = 0.65$)

location of the flame front changed through the cycle; a 'flapping' of the flame front can be observed from the image sequence. As a result of this flame movement, the thickness of the flame brush was observed to increase at phase angles 30°–180°. The very small heat release rate fluctuations in the HRR images at a forcing frequency of 40 Hz are confirmed by the spatially integrated heat release rate shown. The normalized profiles show heat release rate fluctuations of less than 30% around the mean and no trends were observed for any of the forcing amplitudes investigated. However, when the forcing frequency is increased to 310 Hz, large-scale wrinkling of the flame front was observed. The 3rd and 6th row of Fig. 7 shows a full sequence of phase averaged images measured at a forcing frequency of 310 Hz with $A = 0.65$. The first image in this sequence (Fig. 7, $f = 310$ Hz, $\varphi = 0°$) shows the counter-rotating vortex pair wrapping the flame front. Weak heat release rates were observed around the outer vortex which wraps the outer shear layer compared with that of the inner vortex. As the vortices propagate downstream of the bluff-body, they increase in size as can be seen by comparing Fig. 7 ($f = 310$ Hz, $\varphi = 60°$) with Fig. 7 ($f = 310$ Hz, $\varphi = 300°$). In Fig. 7 ($f = 310$ Hz, $\varphi = 210°$), the vortices have propagated along the flame front outside of the region of interest and the wrapping the flame front by another pair of vortices can already be seen close to the bluff-body. The sequence continues in (Fig. 7, $f = 310$ Hz, $\varphi = 240°$ to 330°) with the evolution of another vortex pair at the bluff-body, wrapping the shear layers and the flame front, and propagating away from the bluff-body. Spatially integrated heat release rates for the 310 Hz forcing cycle were calculated, but are not shown here. The profiles show fluctuations of up to 30% around the mean, with a bi-modal profile through the forcing cycle having a local minimum at a phase angle of 180°. The minimum corresponds to $f = 310$ Hz and $\varphi = 180°$ in Fig. 7, where the flame surface is at a minimum. The bimodal shape is due to the high forcing frequency. At this frequency, the vortices propagate at a higher speed compared to lower frequencies. Consequently, the image sequence shown in Fig. 7 (3rd and 6th row), starts with an image showing the vortex pair already wrapping the flame front compared to the image sequence for 160 Hz in Fig. 7 (2nd and 5th row), which starts with the vortex developing at the bluff-body.

3.2 Flame transfer functions

In this section, the periodic heat release rate response of the acoustically forced bluff-body stabilized flame was used in the evaluation of the amplitude and frequency transfer

function $T(f,A)$ (see Eq. 1) for the flame. Transfer functions were evaluated using the HRR as well as OH* chemiluminescence measurements and were then compared.

The work presented in this section aims to demonstrate the capability of the HRR technique in measuring flame transfer functions suitable for use in flame models employed in the prediction of thermoacoustic combustion instabilities. The operating conditions of the bluff-body flame investigated here employs a forcing frequency of 160 Hz and a mean bulk velocity of 9.9 m/s (flame 5). Figure 8 shows a sequence of phase averaged HRR images and Abel-transformed OH* images of the bluff-body flame. Note that as the Abel-transform is performed on averaged OH*-images, which were recorded over a time-scale long enough for the flame to be considered as axis-symmetric over the field-of-view.

The profile of spatially integrated heat release rate corresponding to the Abel-transformed OH* images is shown in Fig. 9a for varying degrees of forcing, $A = 0.12$ to 0.65. The profiles clearly show the cyclic fluctuation of heat release rate through the forcing cycle. A peak occurs at a phase angle of 150° which corresponds to Fig. 8 (2nd row, 150°) where the vortex wrinkles the shear layer and wraps the flame front, thereby reducing the flame surface area. With an increase in forcing amplitude from $A = 0.12$ to 0.52, the peak fluctuation at 150° was observed to increase. With a further increase in A to 0.65, a decrease in the peak was observed. This could be due to a decrease of OH* chemiluminescence signals in regions of high strain and curvature as reported by Najm et al. (1998). Such regions occur during the wrinkling of the flame front and the wrapping of the shear layer by the counter-rotating vortices.

The cyclic heat release rate response of the flame in Fig. 9(b) shows the variation of the spatially integrated heat release rates HRR(t) normalised by the mean HRR through the forcing cycle. The sinusoidal acoustic forcing applied to the flame is also shown in this graph. The profiles of $A = 0.32$, 0.52, 0.65 show a peak heat release rate at a phase angle of 120°; however, for the lowest forcing case ($A = 0.12$), this peak was not observed. As A increases, the wrinkling and wrapping of the flame front intensifies and high negative curvatures are imposed on the flame front. In these regions of negative curvatures, diffusion of free radicals into the fresh reactants increases and as a result an increased local heat release rates has been predicted in calculations (Echekki and Chen 1996). As a result, an increase in the spatially integrated heat release rate was observed in Fig. 9b at phase angles around 120°, where the vortex imposes large-scale structures on the flame front. As expected, the height of the peak increases with increasing forcing amplitude A. An increase of 50% was observed in the peak from $A = 0.12$ to $A = 0.52$, as the wrapping of the flame front in the shear layer intensifies with increasing forcing amplitude. A phase lag between the peaks of the forcing signal and the heat release rate was observed. This is due to the "fuel convection delay time" which refers to the convection time of the premixed reactants from the combustor plenum, where the flow is acoustically forced, to the combustor exit, where the flame is stabilised.

The heat release rate response of the flame as a function of forcing intensity, measured using both HRR and OH* techniques, are compared in Fig. 10a (see Balachandran 2005 for a full description of the calculation of the plotted quantities). The profile of HRR shows a trend of increasing fluctuations with an increase in A, but the profile of OH* is decreasing at $A = 0.65$. This may be due to the decreased OH* fluctuation observed at the highest forcing amplitude as seen in Fig. 9a. However, it must be noted that the process of Abel transforming the OH* raw data introduces artifacts due to noise and further experiments would be needed to confirm this trend conclusively. For example, it is seen on the inverted OH* data in Fig. 8 that there is a changing background level between the different phase angles (which is not apparent on the HRR data, which needs no inversion). If this variation is used as a crude estimator of precision of the OH* measurement, one obtains a precision of the order 20%. The heat release rate trend in Fig. 10a appear to be indicative of a non-linear dependence on forcing, as observed and reported by Bellows and Lieuwen (2004). The fast Fourier transform (see Balachandran et al. 2005) of the heat release rate fluctuations shown in Fig. 10a gives the magnitude and phase of the transfer function T_f which are shown in Fig. 10b and c. The transfer function magnitude for HRR shows a decreasing trend with increasing forcing amplitude, while that for OH* shows an initial decrease followed by an increase in flame response.

4 Flame modeling via uRANS

Preliminary results from uRANS calculations are shown here to demonstrate the use of the experimental data for validation work of computer simulations, work that is ongoing in our laboratories. It is hoped that the current work will stimulate further theoretical investigations on this flame by other groups in the field. Figure 11 shows snapshots taken at phase intervals of 30° of the computed uRANS temperature field at a forcing frequency of 160 Hz and an amplitude of 65%. A direct comparison may be made with the experimental results for temperature, and it is clear that the computational and experimental results are generally in agreement. The prominent vortical structure is well captured by the computation, although its rate of development is noticeably slower than in the experiment.

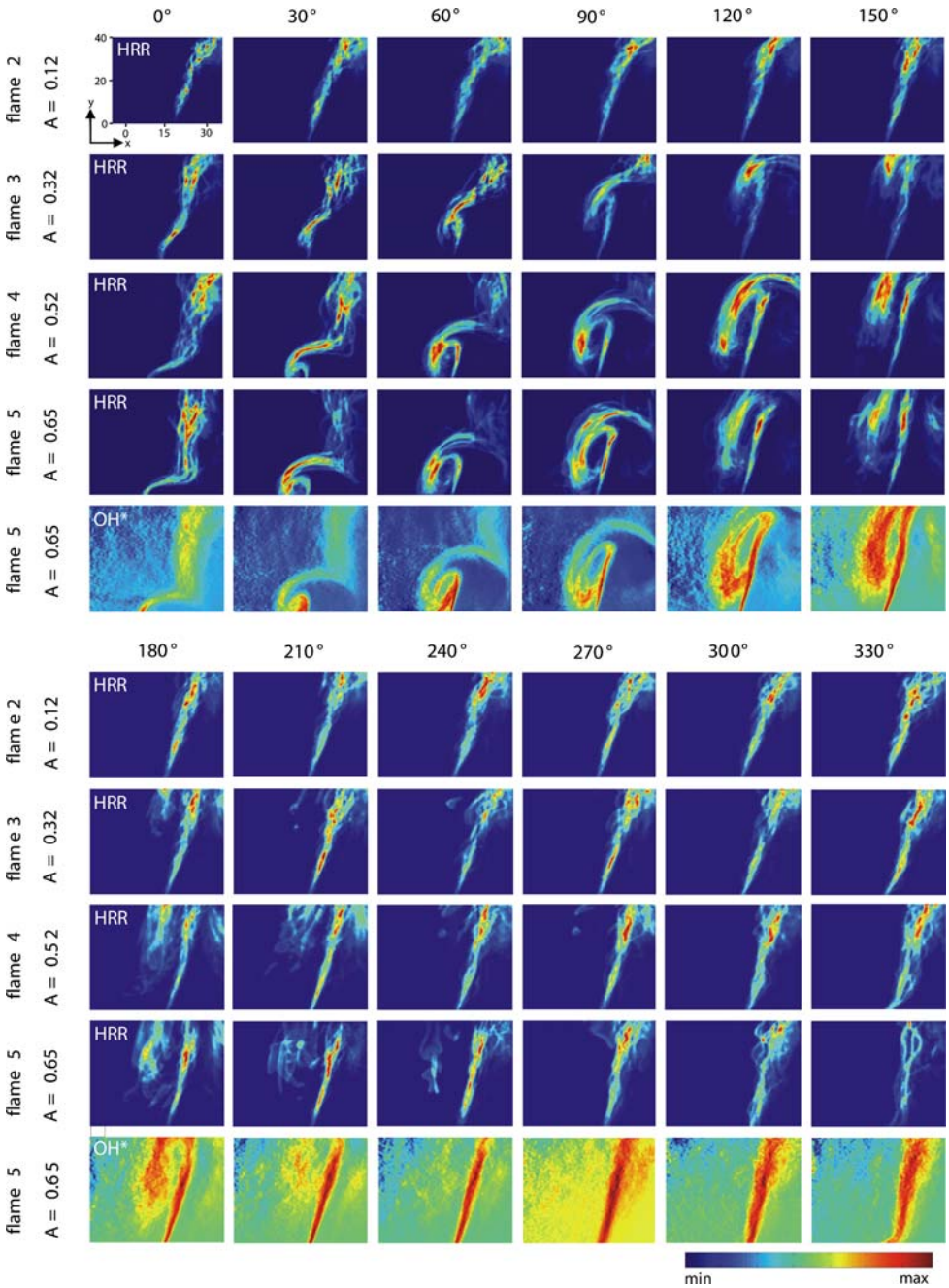

Fig. 8 (Rows 1 to 4 and 6 to 9) A sequence of phase averaged HRR images from the forced bluff-body stabilized flame. Four amplitude fluctuations are investigated (flames 2 to 5; A = 0.12, 0.32, 0.55 and 0.65). A sequence of phase averaged images of Abel-transformed OH* chemiluminescence (flame 5; A = 0.65)

This is probably due to the inlet boundary condition, which was based on the correct overall mass flow rate but did not take into account the non-uniform velocity profile at the inlet plane. Nevertheless the influence of the vortex on the flame is fairly well represented, and over much of the domain the temperature field is in reasonable qualitative agreement.

The experimental results (Fig. 5) shows lower temperatures than the corresponding uRANS results, especially in the outer recirculation region which is susceptible to heat losses to the walls of the enclosure. No model for wall heat transfer was included in the present uRANS formulation which relies on standard wall-functions within the Reynolds stress model. As a consequence the modelled reaction rate is overpredicted in the near-wall region. It is expected that this, together with the inlet boundary condition, can be improved upon in future computational work based at least in part on the present experimental dataset.

5 Conclusions

The periodic response of unsteady turbulent premixed flames was studied using simultaneous PLIF of OH and

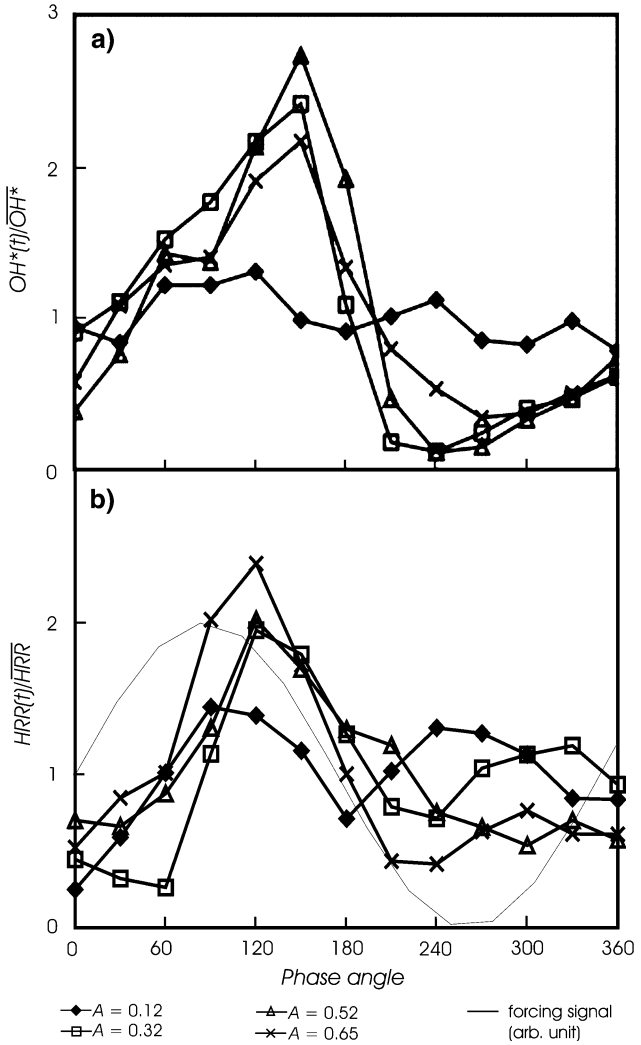

Fig. 9 **a** Cyclic variation of OH*-chemiluminescence in the bluff-body-stabilized flame. The spatially integrated values were normalized by the mean ($\overline{OH^*}$). The profiles were evaluated from OH* images for different amplitude fluctuations (flame 5; A = 0.65). **b** Cyclic variation of heat release rate in the bluff-body-stabilized flame. The spatially integrated values were normalized by the mean ($\overline{HRR}$). The profiles were evaluated from the HRR images for different amplitude fluctuations (flames 2 to 5; A = 0.12, 0.32, 0.55 and 0.65)

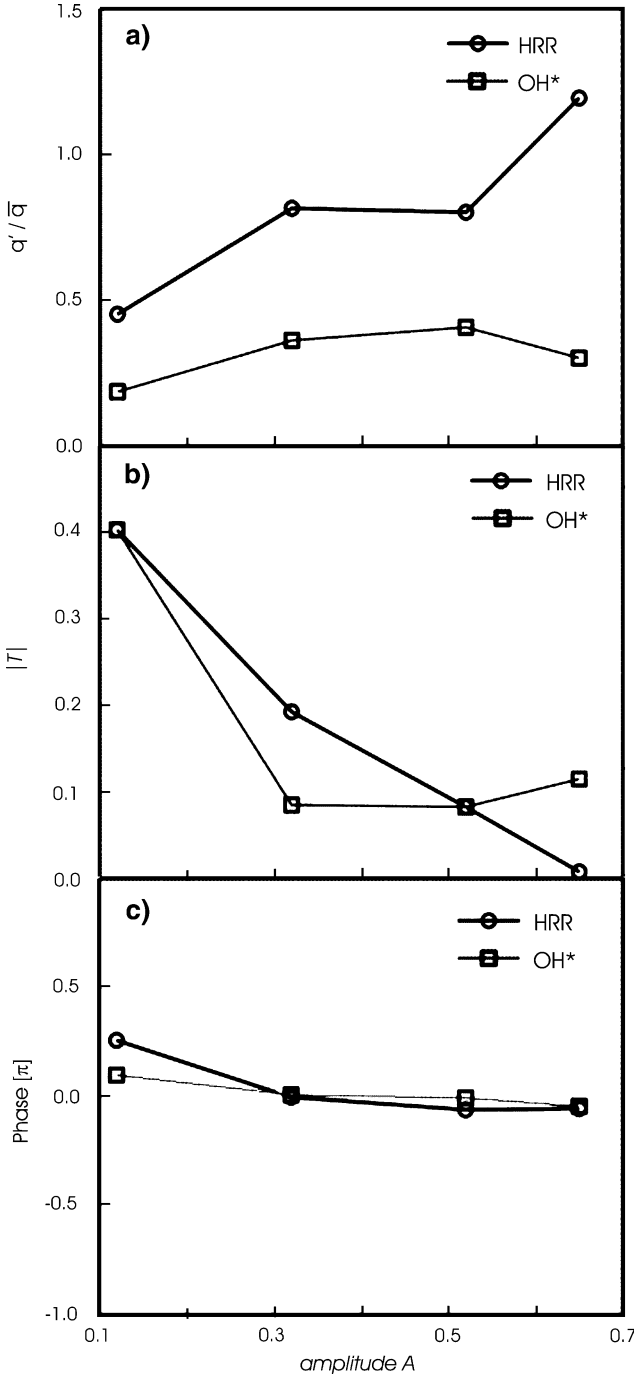

Fig. 10 **a** Heat release rate response of the bluff-body-stabilized flame with increasing amplitude A normalized by the mean ($\overline{q}$). Flame response was measured with OH* chemiluminescence images and resolved phase averaged HRR images (flame 5). Flame transfer function T, evaluated using OH* and HRR for the forced bluff-body stabilized flame. The magnitude (**b**) and phase (**c**) of the transfer function are shown

CH_2O and in a second experiment also two-line thermometry of OH. The amplitude dependence of the heat release rate was investigated by performing measurements at varying degrees of acoustic forcing. Temperature distributions in the bluff-body-stabilised flame were studied and compared to heat release rate measurements made at the same flame conditions. Comparisons were also made with temperature field obtained from uRANS simulations for similar conditions.

Peaks in the fluctuation of heat release rate through the forcing cycle were observed at the phase angle corresponding to the presence of large-scale structures imposed on the flame front by counter-rotating vortices. High heat release rates were observed for highly negatively curved flame fronts, which occur at high amplitudes of forcing. The measured temperature distributions reveal high temperatures around the flame front and around the vortices as

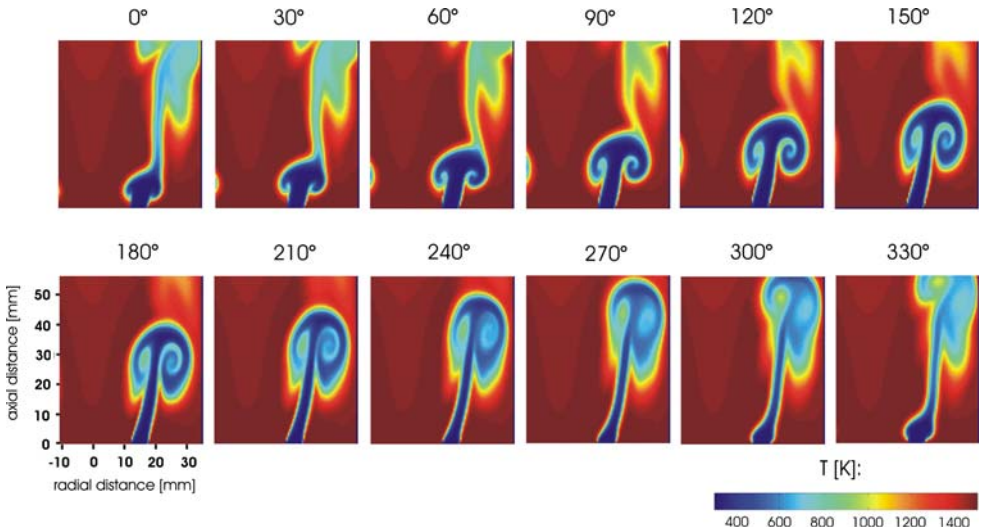

Fig. 11 A sequence of temperature images from uRANS simulations (flame 1, $A = 0.65$)

they wrinkle the flame front. Large regions of high temperature were also observed in the inner recirculation zone for phase angles which correspond to the minimum flame surface area while smaller distributions were observed around the recirculation zone at higher flame surface areas. These features were also observed in the temperature results from uRANS simulations, and this serves to confirm the usefulness of the experimental data-set as a basis for the validation of combustion CFD.

Flame transfer functions evaluated using heat release rate imaging data for a forcing frequency of 160 Hz show a decreasing trend in flame response with increasing amplitude; for measurements performed with OH* chemiluminescence, a decrease followed by an increase was observed for a forcing amplitude of $A = 0.65$. The reduced heat release rate fluctuations observed at the maximum forcing amplitude for OH* chemiluminescence measurements could be due to the sensitivity of OH* to regions of high straining and curvature imposed by the counter-rotating vortices at high forcing amplitudes. The phase of the transfer function measured with both techniques were in good agreement to each other.

The results presented here confirm the capability of the heat release rate imaging technique to measure spatially and temporally resolved heat release rates. The heat release rate imaging technique has here been successfully applied in a preliminary investigation of the non-linear response of turbulent unsteady premixed flames subject to inlet velocity fluctuations, in an effort to study combustion instabilities.

Acknowledgments This work was supported by grants from the EPSRC and grants from Rolls-Royce within INTELLECT D.M. (Integrated lean low emission Combustor design methodology; FP6-502961). BA was supported by a case studentship from Rolls-Royce. GH is grateful to a case studentship from CMI (Cambridge-MIT Institute). JH was supported by an Advanced Research Fellowship from the EPSRC. CFK is thankful to the EPSRC for the provision of a PLATFORM grant and to the Leverhulme trust for personal sponsorship. RSC and CAA acknowledge the financial support of Rolls–Royce and DTI under the ATAP-10 programme. We gratefully acknowledge Dr. J. Frank for many inspiring discussions.

References

Abu-Orf GM (1996), Laminar Flamelet Reaction Rate Modelling for Spark Ignition Engines. PhD thesis, University of Manchester Institute of Science and Technology

Ayoola B (2006) Laser-based measurement of heat release rate and temperature in turbulent premixed flames. PhD thesis, Department of Chemical Engineering, University of Cambridge, Cambridge

Ayoola BO, Balachandran R, Frank JH, Mastorakos E, Kaminski CF (2006) Spatially resolved heat release rate measurements in turbulent premixed flames. Combust Flame 144(1–2):1–16

Armitage CA, Riley AJ, Cant RS, Dowling AP, Stow SR (2004) Flame transfer functions from experiments and CFD. In: ASME TURBO EXPO, 2004-GT-53820

Armitage CA, Balachandran R, Mastorakos E, Cant RS (2006) Investigation of the nonlinear response of turbulent premixed flames to imposed inlet velocity oscillations. Combust Flame 146:419–436

Balachandran R, Ayoola BO, Kaminski CF, Dowling AP, Mastorakos E (2005) Experimental investigation of the nonlinear response of turbulent premixed flames to imposed inlet velocity oscillations. Combust Flame 143(1–2):37–55

Bellows BD, Lieuwen T (2004) Nonlinear response of combustor to forced acoustic oscillations. In: 42nd Aerospace science meeting and exhibit (Reno, NV, USA)

Bray KNC, Libby PA, Moss JB (1985) Unified modelling approach for premixed turbulent combustion. 1. General formulation. Combust Flame 61:87–102

Brookes SJ, Cant RS, Dowling AP (1999) In: ASME TURBO EXPO, 99-GT-112

Brookes SJ, Cant RS, Dowling AP, Dupére IIDJ (2000) In: ASME TURBO EXPO, 2000-GT-0104

Cattolica RJ, Vosen SR (1986) Two-dimensional fluorescence imaging of a flame–vortex interaction. Combust Sci Technol 48(1-2):77–87

Crosley DR (1981) Collisional effects on laser-induced fluorescence flame measurements. Opt Eng 27:511–521

Daly BJ, Harlow FH (1970) Transport equations in turbulence. Phys Fluids 13:2634

Dowling AP, Stow SR (2003) Acoustic analysis of gas turbine combustors. J Propuls Power 19(5):751–764

Dowling AP, Morgans AS (2005) Feedback controll of combustion oscillations. Ann Rev Fluid Mech 37:115–182

Eckbreth AC (1996) Laser diagnostics for combustion temperature and species. Abacus Press, Kent

Echekki T, Chen JH (1996) Unsteady strain rate and curvature effects in turbulent premixed methane–air flames. Combust Flame 116:184–202

Fayouxa A, Zähringer K, Gicquela O, Rolona JC (2005) Experimental and numerical determination of heat release in counterflow premixed laminar flames. Proc Combust Inst 30:251–257

Gaskell PH, Lau AK (1988) Comparison of 2 solution strategies for use with higher-order discretization schemes in fluid flow simulations. Int J Num Meth Fluids 8:617–641

Garland NL, Crosley DR (1986) On the collisional quenching of electronically excited OH, NH, and CH in flames. In: 21st Symposium (international) on combustion. The Combustion Institute, Pittsburg, pp 1693–1702

Giezendanner-Thoben R, Meier U, Meier W, Aigner M (2005a) Phase-locked temperature measurements by two-line OH-PLIF thermometry of a self-excited combustion instability in a gas turbine model combustor. Flow Turbul Combust 75(1–4):317–333

Giezendanner-Thoben R, Meier U, Meier W, Heinze J, Aigner M (2005b) Phase-locked two-line OH planar laser-induced fluorescence thermometry in a pulsating gas turbine model combustor at atmospheric pressure. Appl Opt 44(31):6565–6577

Hartung G (2008) Laser diagnostic investigations of flame turbulence interactions under lean-premixed conditions. PhD thesis, Department of Chemical Engineering, University of Cambridge, Cambridge

Hartung G, Hult J, Kaminski CF, Rogerson J, Swaminathan N (2008) Effect of heat release on turbulence and its interaction with scalar in premixed combustion. Phys Fluids 20:035,110

Issa R (1986) Solution of the implicitely discretized fluid-flow equations by operator-splitting. J Comp Phys 62:40–65

Jambunathan K, Ju XY, Dobbins BN, Ashforthfrost S (1995) An improved cross-correlation technique for particle image velocimetry. Meas Sci Technol 6(5):507–514

Kee RJ, Grcar JF, Smooke MD, Miller JA (1993) A FORTRAN program for modelling steady laminar one-dimensional premixed flames. Sandia National Laboratories Report SAND85-8240

Launder BE, Reece GJ, Rodi W (1975) Progress in development od a Reynolds-stress turbulence closure. J Fluid Mech 68:537–566

Lawn CJ, PoLIFke W (2004) A model for the thermoacoustic response of a premixed swirl burner, Part 2: the flame response. Combust Sci Technol 176(8):1359–1390

Lawn CJ, Evesque S, PoLIFke W (2004) A model for the thermoacoustic response of a premixed swirl burner, Part 1: acoustic aspects. Combustion Science and Technology 176(8):1331–1358

Lee JG, Santavicca D (2003) Experimental diagnostics for the study of combustion instabilities in lean premixed combustors. J Propuls Power 19(5):735–750

Lee T, North GL, Santavicca DA (1993) Surface properties of turbulent premixed propane/air flames at various Lewis numbers. Combust Flame 93:445–456

Li S-P, Cant RS (1994) In: Fourth Biennial UMIST CFD Colloquium

Najm HN, Paul P, Mueller C, Wyckoff PS (1998) On the adequacy of certain experimental observables as measurements of flame burning rate. Combust Flame 113(3):312–332

Palmer JL, Hanson RK (1996) Temperature imaging in a supersonic free jet of combustion gases with two-line OH fluorescence. Appl Opt 35(3):485–499

Paul PH, Najm HN (1998) Planar laser-induced fluorescence imaging of flame heat release rate. In: 27th International combustion symposium. Proc Combust Inst 27:43–50

Pun W, Palm SL, Culick FEC (2003) Combustion dynamics of an acoustically forced flame. Combust Sci Technol 175(3):499–521

Samaniego JM, Egolfopoulos FN, Bowman CT (1995) CO_2* chemiluminescence in premixed flames. Combust Sci Technol 109(1–6):183–203

Tsujishita M, Hirano A, Yokoo M, Sakuraya T, Takeshita Y (1999) Accurate thermometry using NO and OH laser-induced fluorescence in an atmospheric pressure flame (checked by narrow-band N-2 coherent anti-stokes Raman scattering). JSME Int J Ser B Fluids Therm Eng 42(1):119–126

Vagelopoulos CM, Frank JH (2005) An experimental and numerical study on the adequacy of CH as a flame marker in premixed methane flames. Proc Combust Inst 30:241–249

Watkins AP, Li S-P, Cant RS (1996) In: Society of automotive engineers, SAE 961190